Neutron crystalline-electric-field spectroscopy of RPd_2Al_3 (R = Ce, Pr, Nd)

1997 J. Phys.: Condens. Matter 9 5921

(http://iopscience.iop.org/0953-8984/9/27/019)

J. Phys.: Condens. Matter **9** (1997) 5921–5933. Printed in the UK PII: S0953-8984(97)81465-8

Neutron crystalline-electric-field spectroscopy of RPd_2Al_3 (R = Ce, Pr, Nd)

A Dönni†‡, A Furrer†§, H Kitazawa‡ and M Zolliker†‖

† Laboratory for Neutron Scattering, ETH Zürich and Paul Scherrer Institute, CH-5232 Villigen PSI, Switzerland

‡ National Research Institute for Metals, Tsukuba, Ibaraki 305, Japan

Received 31 January 1997

Abstract. The ternary intermetallic compounds RPd_2Al_3 (R = light rare earth) crystallize in the hexagonal $PrNi_2Al_3$-type structure, like the heavy-fermion superconductor UPd_2Al_3. In this paper we present powder neutron scattering and single-crystal magnetic susceptibility experiments on $NdPd_2Al_3$, which provide sufficient information for us to unambiguously determine the crystalline-electric-field (CEF) splitting ($\Gamma_7 \rightarrow \Gamma_9^{(1)} \rightarrow \Gamma_8^{(1)} \rightarrow \Gamma_9^{(2)} \rightarrow \Gamma_8^{(1)}$) of the $^4I_{9/2}$ multiplet of Nd^{3+}. The CEF parameters obtained for $NdPd_2Al_3$ are extrapolated to those for $PrPd_2Al_3$ and $CePd_2Al_3$. For $PrPd_2Al_3$, the powder neutron scattering measurement of the two strongest CEF excitations confirms the reliability of the extrapolated CEF level diagram ($\Gamma_1 \rightarrow \Gamma_5 \rightarrow \Gamma_6^{(1)} \rightarrow \Gamma_3 \rightarrow \Gamma_4 \rightarrow \Gamma_6^{(2)}$) with an accuracy of better than 10% for the excitation energies. For $CePd_2Al_3$, with a rather strong Kondo effect, the extrapolation yields a CEF level sequence ($\Gamma_7 \rightarrow \Gamma_9 \rightarrow \Gamma_8$) similar to that derived from single-crystal susceptibility data, and the predicted $\Gamma_7 \rightarrow \Gamma_9$ excitation energy lies well inside the width of the broad inelastic magnetic peak observed by neutron scattering. The CEF parameters yield a magnetic anisotropy which is compatible with the magnetic structures observed in $CePd_2Al_3$ and $NdPd_2Al_3$, and predict no magnetic ordering for $PrPd_2Al_3$ down to the lowest temperatures.

1. Introduction

Like the heavy-fermion superconductor UPd_2Al_3, the rare-earth intermetallic compounds RPd_2Al_3 (R = Ce, Pr, Nd, Sm, Gd) adopt the hexagonal $PrNi_2Al_3$-type crystal structure, shown in figure 1, which consists of Pr–Ni layers, alternating along the *c*-direction with isolated Al layers. In UPd_2Al_3 [1, 2] ($\gamma = 150$ mJ K^{-2} mol^{-1}, $T_c = 2$ K, $T_N = 14$ K), superconductivity coexists with a quite large antiferromagnetically ordered uranium moment of 0.85 μ_B. $CePd_2Al_3$ [3, 4] has been characterized as an antiferromagnetically ordered heavy-fermion compound ($\gamma = 380$ mJ K^{-2} mol^{-1}, $T_N = 2.8$ K), which is located very close to the magnetic-to-nonmagnetic boundary in the Kondo-lattice phase diagram. $PrPd_2Al_3$ [5] remains paramagnetic down to 1.5 K, and $NdPd_2Al_3$ [6] shows antiferromagnetism below $T_N = 7.7$ K. Multiple magnetic phase transitions have been observed for $SmPd_2Al_3$ [7] at $T_1 = 12$ K, $T_2 = 4.3$ K, and $T_3 = 4.0$ K, and for $GdPd_2Al_3$ [8, 9] at $T_1 = 16$ K and $T_2 = 13$ K, but the magnetic structures have not yet been determined. The relevant structural and magnetic parameters are summarized in table 1. For $CePd_2Al_3$,

§ Author to whom any correspondence should be addressed: Professor Dr Albert Furrer, Laboratory for Neutron Scattering, ETH Zürich & Paul Scherrer Institute, CH-5232 Villigen PSI, Switzerland; fax: (+41)-56-3102939; phone: (+41)-56-3102088; e-mail: Albert.Furrer@psi.ch.

‖ Present address: Institut Laue–Langevin, BP 156, F-38042 Grenoble, France.

0953-8984/97/275921+13$19.50

$NdPd_2Al_3$, and UPd_2Al_3 the ordered magnetic moments are oriented perpendicularly to the hexagonal *c*-axis and perpendicularly to the respective propagation vector. The coupling of the magnetically ordered moments is either ferromagnetic in the basal plane and antiferromagnetic along the *c*-direction (the propagation vector $\boldsymbol{k} = [0, 0, 1/2]$ in $CePd_2Al_3$ and UPd_2Al_3), or antiferromagnetic in the *ab*-plane and ferromagnetic along the *c*-axis (the propagation vector $\boldsymbol{k} = [1/2, 0, 0]$ in $NdPd_2Al_3$).

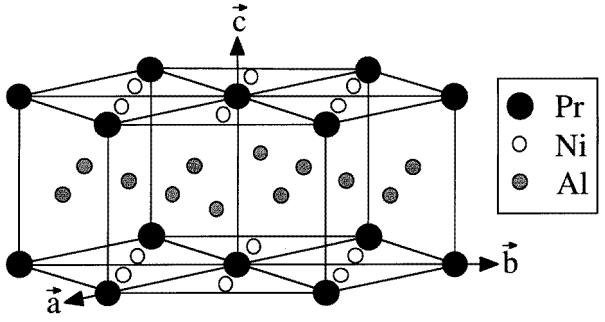

Figure 1. The $PrNi_2Al_3$-type crystal structure; hexagonal space group $P6/mmm$ (No 191) with sites 1a occupied by Pr, 2c by Ni, and 3g by Al.

Table 1. Room temperature lattice parameters (a, c) and magnetic structures of the compounds RPd_2Al_3 (R = Ce, Pr, Nd, Sm, Gd) and UPd_2Al_3, all with hexagonal $PrNi_2Al_3$-type crystal structure. T_N: Néel temperature; $\boldsymbol{k}$: magnetic propagation vector; μ_0: ordered magnetic saturation moment with direction $\boldsymbol{\mu}$; ?: not yet determined.

Compound	$CePd_2Al_3$	$PrPd_2Al_3$	$NdPd_2Al_3$	$SmPd_2Al_3$	$GdPd_2Al_3$	UPd_2Al_3
References	[3, 10]	This work	[6]	[7]	[8, 9]	[1, 2]
a (Å)	5.4709(4)	5.4569(5)	5.4419(1)	5.4131(1)	5.3924(9)	5.365
c (Å)	4.2157(4)	4.2117(6)	4.2069(1)	4.1997(1)	4.1941(4)	4.186
c/a	0.7706(2)	0.7718(2)	0.7731(1)	0.7758(1)	0.7778(2)	0.780
T_N (K)	2.8(1)	No order	7.7(1)	12, 4.3, 4.0	16, 13	14
$\boldsymbol{k}$	[0, 0, 1/2]	—	[1/2, 0, 0]	?	?	[0, 0, 1/2]
μ_0 (μ_B)	0.47(2)	—	2.28(7)	?	?	0.85(3)
	$\boldsymbol{\mu} \perp \boldsymbol{c}$	—	$\boldsymbol{\mu} \perp \boldsymbol{c}$	?	?	$\boldsymbol{\mu} \perp \boldsymbol{c}$
	$\boldsymbol{\mu} \perp \boldsymbol{k}$	—	$\boldsymbol{\mu} \perp \boldsymbol{k}$	?	?	$\boldsymbol{\mu} \perp \boldsymbol{k}$

The physical and magnetic properties of RPd_2Al_3 compounds depend strongly on the sample preparation procedures. Samples of better quality (defined as structural closeness to the ideal $PrNi_2Al_3$-type lattice) are characterized by smaller lattice constants and higher values of the Néel temperature T_N. For $NdPd_2Al_3$, T_N exhibits a linear dependence on the lattice parameter a [6], and the value $T_N = 5.3$ K obtained for the best single-crystalline sample is significantly reduced to below the value of $T_N = 7.7$ K for the best polycrystalline sample. For $CePd_2Al_3$, a slightly randomized exchange coupling introduced by site disorder and vacancies in the single-crystalline [11] and splat-cooled polycrystalline [4] samples may account for the observed disappearance of the long-range magnetic order.

For an understanding of the magnetism in the RPd_2Al_3 compounds on a microscopic scale, knowledge of the crystalline-electric-field (CEF) interaction is indispensable. We have performed powder neutron scattering and single-crystal susceptibility experiments on $NdPd_2Al_3$ in order to determine the CEF splitting of the $^4I_{9/2}$ multiplet of Nd^{3+}. The CEF level diagrams of $PrPd_2Al_3$ and $CePd_2Al_3$, obtained by an extrapolation from that for $NdPd_2Al_3$, are compared with additional powder neutron scattering experiments performed

on $PrPd_2Al_3$, and with single-crystal susceptibility and powder neutron scattering data on $CePd_2Al_3$ reported in the literature [11, 12].

2. Experimental details

The polycrystalline $NdPd_2Al_3$ and $PrPd_2Al_3$ samples for the neutron scattering experiments were synthesized by arc melting the pure elements (Nd: 3N; Pr: 3N; Pd: 4N; Al: 5N) with starting compositions Nd:Pd:Al of 1:2:3 and Pr:Pd:Al of 1.005:2:3.03 in an argon atmosphere under continuous titanium gettering, and were annealed at 900 °C for 120 hours in high vacuum. The $NdPd_2Al_3$ single crystal for the susceptibility experiment was prepared from a melt of an aluminium-rich sample a with a Nd:Pd:Al starting composition of 1:2:3.03 in the same tri-arc furnace by the Czochralsky pulling method, and was not annealed. Nonstoichiometric compositions of the starting material are chosen to compensate the evaporation of mainly aluminium during the process of sample preparation (for details, see [6]). The x-ray diffraction patterns of all of the $NdPd_2Al_3$ and $PrPd_2Al_3$ samples can be completely indexed with the hexagonal $PrNi_2Al_3$-type structure, and traces of possible impurity phases are limited to well below 1% of the observed total Bragg intensities. The two $NdPd_2Al_3$ samples have previously been used in the investigation of the sample dependence of magnetic properties [6], and correspond to the best polycrystalline sample, named PC1 in [6], with $T_N = 7.7$ K, and to the single crystal named SC2a in [6], with $T_N = 5.2$ K. For the $PrPd_2Al_3$ sample with the lattice parameters given in table 1, the absence of magnetic ordering was confirmed down to 1.5 K.

The inelastic neutron scattering measurements were carried out on the triple-axis spectrometer IN3 at the Institut Laue–Langevin, Grenoble, France, for energy transfers up to 36 meV. In order to achieve a gain in intensity, a horizontally and vertically focusing monochromator (copper (1, 1, 1) and graphite (0, 0, 2)) and a horizontally focusing analyser (graphite (0, 0, 2)) were used. Constant-$\boldsymbol{Q}$ scans were performed for moduli of the scattering vector $\boldsymbol{Q}$ in the range 0.8 $\text{Å}^{-1} < Q < 4.5$ Å^{-1}, and the energy of the scattered neutrons E_f fixed at 13.7 meV, and 4.80 meV. For $E_f = 13.7$ meV a pyrolytic graphite filter was placed in the scattered neutron beam in order to reduce higher-order contamination, while for $E_f = 4.80$ meV a beryllium filter was used for the same reason. The energy resolution at the elastic peak ($\Delta E = 0$) turned out to be $\delta E = 0.12$ meV for $E_f = 4.80$ meV, and $\delta E = 0.47$ meV for $E_f = 13.7$ meV. The $NdPd_2Al_3$ and $PrPd_2Al_3$ powder samples were filled under a helium gas atmosphere into aluminium cylinders of diameter 10 mm and height 50 mm, and mounted in a closed-cycle He refrigerator to achieve temperatures between 10 K and 300 K.

The magnetic dc susceptibility $\chi \equiv M/H$ was measured parallel and perpendicular to the hexagonal c-axis of the $NdPd_2Al_3$ single crystal down to 1.9 K in an external field of 0.1 T by using a SQUID magnetometer (Quantum Design).

3. Results and discussion

3.1. CEF levels in $NdPd_2Al_3$

The CEF Hamiltonian of hexagonal symmetry

$$H_{CEF} = B_{20}O_2^0 + B_{40}O_4^0 + B_{60}O_6^0 + B_{66}O_6^6 \tag{1}$$

where the B_{nm} are the CEF parameters and the O_n^m are operator equivalents built from spin operators [13], gives rise to a decomposition of the tenfold-degenerate ground-state

Table 2. CEF parameters (B_{nm}), eigenfunctions (Γ_i), energies (E_i), and transition probabilities ($|\langle\Gamma_i|J_\perp|\Gamma_j\rangle|^2$) for $NdPd_2Al_3$ obtained from a fit to the powder neutron scattering and single-crystal magnetic susceptibility data. Bold numbers correspond to CEF transitions with zero energy transfer.

CEF parameters B_{nm}:	(Fit)
B_{20} (meV)	0.214 ± 0.005
B_{40} (10^{-2} meV)	-0.105 ± 0.002
B_{60} (10^{-4} meV)	-0.224 ± 0.006
B_{66} (10^{-3} meV)	0.438 ± 0.021

Eigenfunctions Γ_i: (calculated)	Energies E_i (meV): (calculated)	(observed)
$\Gamma_8^{(2)} = 0.288\|\pm5/2\rangle + 0.958\|\mp7/2\rangle$	12.24	12.24 ± 0.15
$\Gamma_9^{(2)} = 0.133\|\pm3/2\rangle + 0.991\|\mp9/2\rangle$	11.80	11.8 ± 0.3
$\Gamma_8^{(1)} = 0.958\|\pm5/2\rangle - 0.288\|\mp7/2\rangle$	4.24	4.24 ± 0.05
$\Gamma_9^{(1)} = 0.991\|\pm3/2\rangle - 0.133\|\mp9/2\rangle$	0.83	0.83 ± 0.03
$\Gamma_7 = \|\pm1/2\rangle$	0	0

Transition probabilities $\|\langle\Gamma_i\|J_\perp\|\Gamma_j\rangle\|^2$: (calculated) E (meV)	Γ_7 0	$\Gamma_9^{(1)}$ 0.83	$\Gamma_8^{(1)}$ 4.24	$\Gamma_9^{(2)}$ 11.80	$\Gamma_8^{(2)}$ 12.24
$\Gamma_8^{(2)}$					**15.26**
$\Gamma_9^{(2)}$				**25.74**	6.09
$\Gamma_8^{(1)}$			**8.59**	0.05	11.07
$\Gamma_9^{(1)}$		**2.59**	13.29	0.83	0.57
Γ_7	**17.00**	15.72	0	0.28	0

J-multiplet $^4I_{9/2}$ of Nd^{3+} in $NdPd_2Al_3$ into five doublets ($\Gamma_7, \Gamma_8^{(1)}, \Gamma_8^{(2)}, \Gamma_9^{(1)}, \Gamma_9^{(2)}$). The interpretation of neutron spectroscopic data requires the identification of the observed CEF states with energy E_i with their correct representations Γ_i. This is usually achieved by comparing the observed intensities of the CEF transitions $|\Gamma_i\rangle \rightarrow |\Gamma_j\rangle$ with the differential neutron cross section, which for a system with N noninteracting ions is given in the dipole approximation by [14]

$$\frac{d^2\sigma}{d\Omega\, d\omega} = \frac{N}{Z}\left(\frac{\gamma e^2}{m_e c^2}\right)\frac{k_1}{k_0}\exp[-2W(\boldsymbol{Q})]F^2(\boldsymbol{Q})\exp[-E_i k_B T] \times |\langle\Gamma_i|J_\perp|\Gamma_j\rangle|^2\delta(E_i - E_j + \hbar\omega). \quad (2)$$

Z is the partition function, k_0 and k_1 are the wavenumbers of the incoming and scattered neutrons, respectively, $\exp[-2W]$ is the Debye–Waller factor, $F(\boldsymbol{Q})$ the magnetic form factor, and $J_\perp$ the component of the total angular momentum operator perpendicular to the scattering vector $\boldsymbol{Q}$. The remaining symbols have their usual meaning. The intensities of the CEF transitions are decreasing with increasing scattering vector due to the form factor, and their temperature dependence is governed by Boltzmann statistics.

From the evidence described below, our experiments suggest the CEF diagram for $NdPd_2Al_3$ shown in figure 2, which gives rise to the values of the CEF parameters (B_{20}, B_{40}, B_{60}, B_{66}), and the calculated eigenfunctions (Γ_i), energies (E_i), and transition probabilities

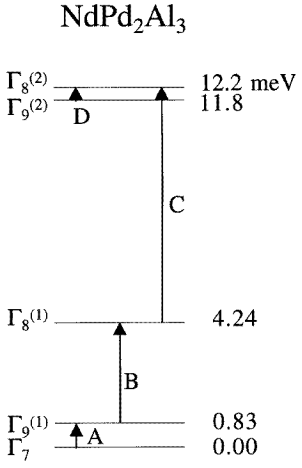

Figure 2. The CEF level diagram for $NdPd_2Al_3$ derived from powder neutron scattering and single-crystal magnetic susceptibility data. Arrows indicate CEF transitions with large transition probabilities (see table 2).

($|\langle\Gamma_i|J_\perp|\Gamma_j\rangle|^2$) given in table 2. The four inelastic CEF transitions with large transition probabilities (see table 2) are indicated by arrows in figure 2.

The IN3 energy spectra of paramagnetic $NdPd_2Al_3$, shown in figure 3, exhibit three inelastic lines, which appear for neutron energy loss (A, B, C) and for neutron energy gain (A′, B′). The excitations A at 0.83 ± 0.03 meV, B at 3.41 ± 0.02 meV and C at 8.0 ± 0.1 meV have all been confirmed to be of magnetic origin by measurements with larger scattering vectors $\boldsymbol{Q}$. Upon increasing the temperature from 15 to 40 K, the intensity is decreasing for the line A and increasing for the excitations B and C. Thus, the unresolved shoulder A can immediately be identified as a ground-state CEF transition, whereas the lines B and C are excited-state CEF transitions. When assuming for $NdPd_2Al_3$ a CEF ground state Γ_7, it is straightforward (see the arrows in figure 2) to interpret the lines A, B, and C as the $\Gamma_7 \rightarrow \Gamma_9^{(1)}$, $\Gamma_9^{(1)} \rightarrow \Gamma_8^{(1)}$, and $\Gamma_8^{(1)} \rightarrow \Gamma_8^{(2)}$ transitions, respectively. Figure 4 displays an IN3 spectrum under improved resolution conditions. The magnetic scattering near the elastic line contains contributions from the inelastic CEF transitions A ($\Gamma_7 \rightarrow \Gamma_9^{(1)}$) and A′ ($\Gamma_9^{(1)} \rightarrow \Gamma_7$) as well as from the elastic CEF transitions $\Gamma_9^{(1)} \rightarrow \Gamma_9^{(1)}$ and—mainly—$\Gamma_7 \rightarrow \Gamma_7$ (see the transition probabilities in table 2), which all appear broader than the instrumental resolution indicated by the dashed line.

Since the IN3 spectra measured at higher temperatures failed to exhibit the CEF transition D (see figure 2), the energy of $\Gamma_9^{(2)}$ remains undetermined. Figure 5 displays the values of the CEF parameters B_{20}, B_{40}, B_{60}, and B_{66} of $NdPd_2Al_3$ as functions of $E(\Gamma_9^{(2)})$, with the energies $E(\Gamma_7)$, $E(\Gamma_9^{(1)})$, $E(\Gamma_8^{(1)})$, and $E(\Gamma_8^{(2)})$ fixed at the values observed by means of neutron scattering. Such a fit has only one free parameter, $E(\Gamma_9^{(2)})$, and all of the sets of B_{nm}-parameters reproduce the correct energies of the other four CEF levels.

We now proceed to compare the magnetic susceptibility calculated for the different sets of B_{nm} of figure 5 with the susceptibility measured parallel ($\|\boldsymbol{c}$) and perpendicular ($\perp\boldsymbol{c}$) to the hexagonal c-axis of the $NdPd_2Al_3$ single crystal. As shown in the upper frame of figure 6, the calculations give the correct magnetic anisotropy, and the observed χ^{-1} ($\|\boldsymbol{c}$) data allow a precise estimation to be made of the energy: $E(\Gamma_9^{(2)}) = 11.8 \pm 0.3$ meV. The agreement between the observed magnetic susceptibility χ ($\perp c$) and the calculated susceptibility χ_{CEF} = calc(11.8) can be further improved by including the effects of magnetic exchange interactions between Nd ions. For $NdPd_2Al_3$, a fit of the susceptibility χ_M (see the lower frame of figure 6), which in the molecular-field approximation [15] is

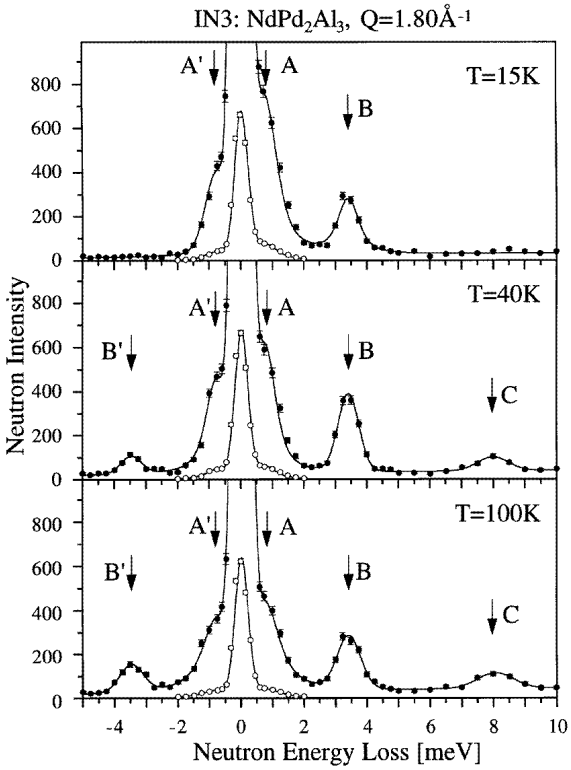

Figure 3. IN3 energy spectra at $T = 15$, 40, and 100 K of neutrons scattered from polycrystalline $NdPd_2Al_3$ for $Q = 1.80$ Å^{-1} and fixed $E_f = 13.7$ meV. Open symbols show the neutron intensity divided by 10. The curve corresponds to the fit of the total scattering, and letters refer to CEF transitions of the diagram shown in figure 2.

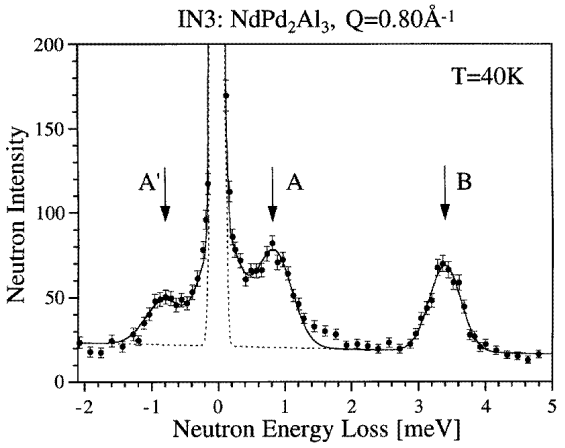

Figure 4. The high-resolution IN3 energy spectrum at $T = 40$ K of neutrons scattered from polycrystalline $NdPd_2Al_3$ for $Q = 0.80$ Å^{-1} and fixed $E_f = 4.80$ meV. The dashed line indicates the spectrometer resolution at $\Delta E = 0$ meV. The curve corresponds to the fit of the total scattering, and letters refer to CEF transitions of the diagram shown in figure 2.

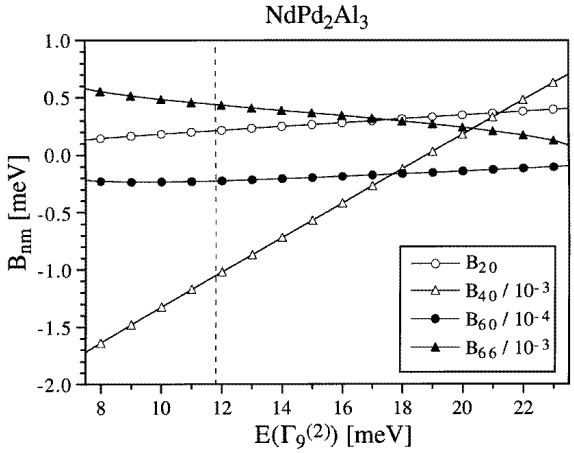

Figure 5. Values of the CEF parameters B_{20}, B_{40}, B_{60}, and B_{66} of $NdPd_2Al_3$ as functions of $E(\Gamma_9^{(2)})$, with the energies of the other four CEF levels fixed at $E(\Gamma_7) = 0$ meV, $E(\Gamma_9^{(1)}) = 0.83$ meV, $E(\Gamma_8^{(1)}) = 4.24$ meV, and $E(\Gamma_8^{(2)}) = 12.24$ meV. The dashed line at $E(\Gamma_9^{(2)}) = 11.8$ meV marks the best set of CEF parameters based on single-crystal susceptibility data.

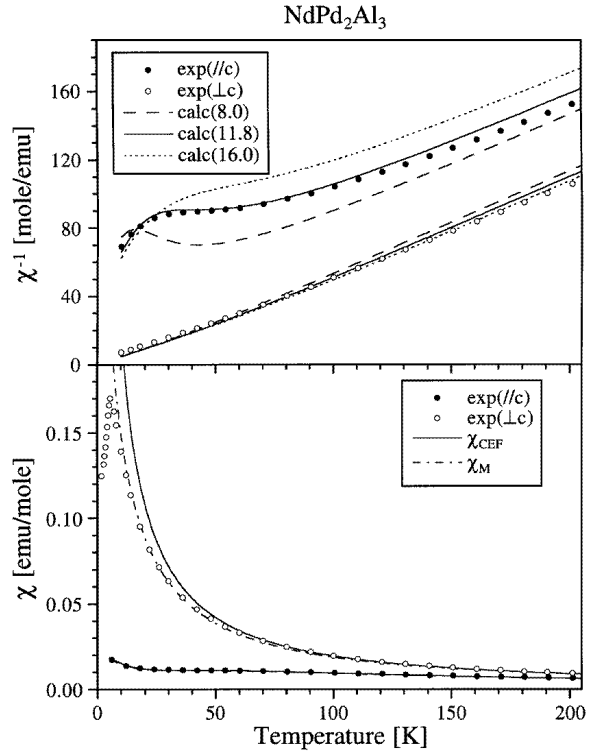

Figure 6. The single-crystal magnetic susceptibility of $NdPd_2Al_3$ measured parallel and perpendicular to the hexagonal c-axis. The calculations calc($E(\Gamma_9^{(2)})$ in meV), are based on the CEF parameters of figure 5. $\chi_{CEF} =$ calc(11.8). The curve for χ_M was obtained by a fit of equation (3).

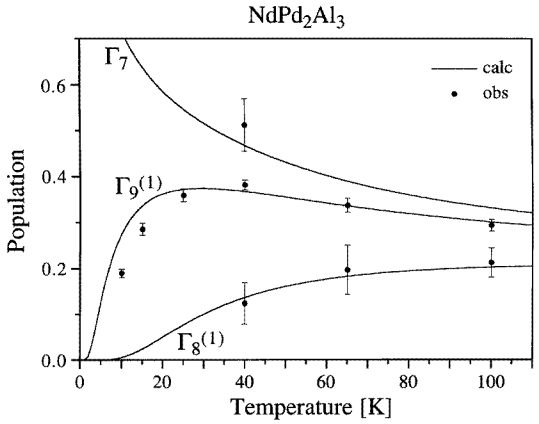

Figure 7. Calculated (solid lines) and observed (black dots) temperature dependences of the populations of the CEF levels Γ_7, $\Gamma_9^{(1)}$, and $\Gamma_8^{(1)}$ of $NdPd_2Al_3$.

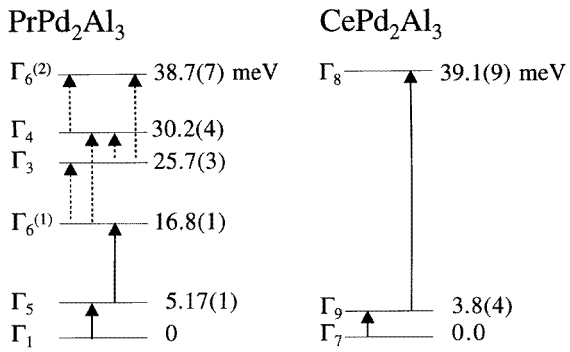

Figure 8. CEF level diagrams for $PrPd_2Al_3$ and $CePd_2Al_3$ extrapolated from that of $NdPd_2Al_3$. Arrows indicate CEF transitions with large (solid line) and intermediate (dashed line) transition probabilities (see tables 3 and 4).

given by

$$\chi_M = \chi_{CEF}/(1 - \lambda\chi_{CEF}) \tag{3}$$

yields an exchange coupling parameter $\lambda = -2.0$ mol emu^{-1} indicating antiferromagnetic exchange interactions. The CEF transition D ($\Gamma_9^{(2)} \rightarrow \Gamma_8^{(2)}$) has not been observed via neutron scattering because of the small excitation energy (<1 meV). The CEF diagram of figure 2 is compatible with the observed neutron intensities: at 40 K the ratio Int(B)/Int(A) becomes 0.66 (calculated) and 0.7(2) (observed; figure 4), whereas the ratio Int(C)/Int(B) becomes 0.31 (calculated) and 0.3(1) (observed; figure 3). The temperature dependences of the observed and calculated populations of the CEF levels Γ_7, $\Gamma_9^{(1)}$, and $\Gamma_8^{(1)}$ are compared in figure 7.

For the CEF ground-state doublet Γ_7 of $NdPd_2Al_3$, the expected ordered moments are 1.82 μ_B for the basal plane and 0.36 μ_B parallel to the *c*-axis. The large magnetic anisotropy of Γ_7 fixes the directions of the antiferromagnetically ordered Nd moments into the basal plane. In $NdPd_2Al_3$, the strength of the magnetic exchange interactions ($T_N = 7.7$ K) is comparable to the energy separation ($\Delta E = 9.6(4)$ K) of the two lowest-

Table 3. CEF parameters (B_{nm}), eigenfunctions (Γ_i), energies (E_i), and transition probabilities ($|\langle\Gamma_i|J_\perp|\Gamma_j\rangle|^2$) for $PrPd_2Al_3$ obtained by an extrapolation from those of $NdPd_2Al_3$. Bold numbers correspond to CEF transitions with zero energy transfer.

CEF parameters B_{nm}:	(Extrapolation)
B_{20} (meV)	0.758 ± 0.018
B_{40} (10^{-2} meV)	-0.312 ± 0.006
B_{60} (10^{-4} meV)	0.458 ± 0.012
B_{66} (10^{-3} meV)	-0.894 ± 0.043

Eigenfunctions Γ_i: (extrapolated)	Energies E_i (meV): (extrapolated)	(observed)
$\Gamma_6^{(2)} = 0.078\|\pm2\rangle - 0.997\|\mp4\rangle$	38.7 ± 0.7	—
$\Gamma_4 = 0.707\|+3\rangle - 0.707\|-3\rangle$	30.2 ± 0.4	—
$\Gamma_3 = 0.707\|+3\rangle + 0.707\|-3\rangle$	25.7 ± 0.3	—
$\Gamma_6^{(1)} = 0.997\|\pm2\rangle + 0.078\|\mp4\rangle$	16.8 ± 0.1	16.82 ± 0.05
$\Gamma_5 = \|\pm1\rangle$	5.17 ± 0.01	5.50 ± 0.01
$\Gamma_1 = \|0\rangle$	0	0

Transition probabilities $\|\langle\Gamma_i\|J_\perp\|\Gamma_j\rangle\|^2$: (extrapolated)	Γ_1	Γ_5	$\Gamma_6^{(1)}$	Γ_3	Γ_4	$\Gamma_6^{(2)}$
E (meV)	0	5.17	16.8	25.7	30.2	38.7
$\Gamma_6^{(2)}$						**20.94**
Γ_4					**0**	3.23
Γ_3				**0**	6.00	2.13
$\Gamma_6^{(1)}$			**5.14**	5.20	4.10	0.29
Γ_5		**1.33**	11.93	0	0	0.07
Γ_1	**0**	13.33	0	0	0	0

lying CEF doublets, Γ_7 and $\Gamma_9^{(1)}$. Thus, the enhancement of the observed saturation moment $\mu_0(\mathrm{Nd}) = 2.28(7)\ \mu_B$ [6] above the value $1.82\ \mu_B$ expected for Γ_7 reflects the mixing of $\Gamma_9^{(1)}$ into the ground-state singlet of the antiferromagnetically ordered state of $NdPd_2Al_3$. In fact, a mean-field calculation including the full CEF level scheme yields $\mu_0(\mathrm{Nd}) = 2.53\ \mu_B$, with $\lambda = -2.0$ mol emu^{-1}.

3.2. Extrapolation to $PrPd_2Al_3$

The CEF parameters determined for $NdPd_2Al_3$ can be extrapolated to those of other trivalent rare-earth ions R with the same chemical structure RPd_2Al_3, since the CEF parameters then essentially scale with $\langle r^n\rangle$, the nth moment of the radial distribution of the 4f electrons, and with χ_n, the reduced matrix elements or Stevens factors [16]:

$$B_{nm}(\mathrm{R}) \;=\; B_{nm}(\mathrm{Nd})\,\frac{\langle r^n\rangle(\mathrm{R})}{\langle r^n\rangle(\mathrm{Nd})}\,\frac{\chi_n(\mathrm{R})}{\chi_n(\mathrm{Nd})}. \tag{4}$$

For $PrPd_2Al_3$, the CEF Hamiltonian (1) splits the ninefold-degenerate ground-state J-multiplet $^3H_4$ of Pr^{3+} into three singlets ($\Gamma_1, \Gamma_3, \Gamma_4$) and three doublets ($\Gamma_5, \Gamma_6^{(1)}, \Gamma_6^{(2)}$). The extrapolation (4) with no adjustable parameter yields the CEF level diagram shown in figure 8 with the CEF parameters, eigenfunctions, energies, and transition probabilities given

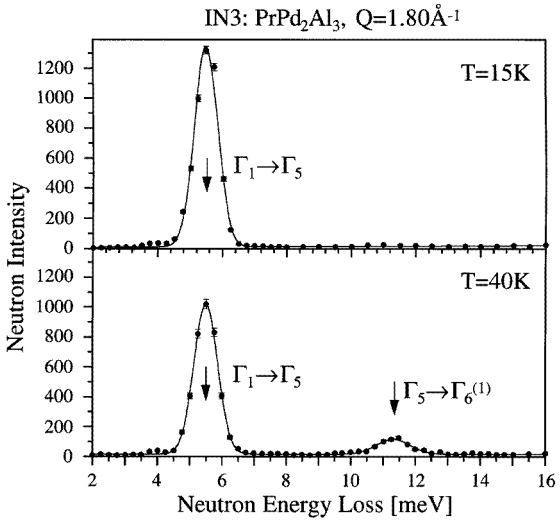

Figure 9. IN3 energy spectra at $T = 15$ and 40 K of neutrons scattered from polycrystalline $PrPd_2Al_3$ for $Q = 1.80$ Å^{-1} and fixed $E_f = 13.7$ meV. The curve corresponds to the fit of the total scattering.

in table 3. The CEF ground state of $PrPd_2Al_3$ is predicted to be the nonmagnetic singlet Γ_1, which is separated from the first excited state (doublet Γ_5) by 5.17 ± 0.01 meV, and from the second excited state (doublet $\Gamma_6^{(1)}$) by 16.8 ± 0.1 meV. The two CEF transitions $\Gamma_1 \rightarrow \Gamma_5$ and $\Gamma_5 \rightarrow \Gamma_6^{(1)}$, marked by solid-line arrows in figure 8, have the largest transition probabilities (see table 3). IN3 neutron scattering spectra of $PrPd_2Al_3$ are shown in figure 9. At 15 K, only one intense inelastic line, at 5.50 ± 0.01 meV, is observed. At 40 K, the intensity of the dominant line is reduced, and a weaker excitation shows up at 11.32 ± 0.04 meV. The magnetic origin of both excitations has been verified by means of measurements with larger scattering vectors $\boldsymbol{Q}$. Guided by the extrapolation (figure 8), we associate the intense line with the ground-state transition $\Gamma_1 \rightarrow \Gamma_5$ and the weaker line with the excited-state transition $\Gamma_5 \rightarrow \Gamma_6^{(1)}$. The predicted excitation energies are in good agreement with the experimental data: only 6% smaller than observed for $\Gamma_1 \rightarrow \Gamma_5$ and only 3% larger than observed for $\Gamma_5 \rightarrow \Gamma_6^{(1)}$. Furthermore, the predicted intensities are in agreement with the experiment: for $\Gamma_1 \rightarrow \Gamma_5$, the ratio $\mathrm{Int}(T = 40\ \mathrm{K})/\mathrm{Int}(T = 15\ \mathrm{K})$ becomes 0.72 (calculated) and 0.8(1) (observed; figure 9), whereas at 40 K, the ratio $\mathrm{Int}(\Gamma_5 \rightarrow \Gamma_6^{(1)})/\mathrm{Int}(\Gamma_1 \rightarrow \Gamma_5)$ becomes 0.18 (calculated) and 0.1(1) (observed; figure 9). Our powder neutron scattering measurement of the two strongest CEF transitions confirms the reliability of the extrapolated CEF level diagram of $PrPd_2Al_3$ (figure 8), with an accuracy of better than 10% for the excitation energies. A verification of the weaker CEF transitions of $PrPd_2Al_3$ (see the dashed-line arrows in figure 8) might be possible by means of a future single-crystal neutron scattering experiment.

The magnetically easy axis of $PrPd_2Al_3$ lies inside the hexagonal ab-plane, like those of $NdPd_2Al_3$ and $CePd_2Al_3$. Due to the large energy separation $\Gamma_1 \rightarrow \Gamma_5$ of 64 K (5.50 meV), no magnetic ordering is expected for $PrPd_2Al_3$ down to the lowest temperatures. An estimation of the magnetic entropy from specific heat data for $PrPd_2Al_3$ [17] supports the CEF diagram of figure 8 by suggesting a singlet as the CEF ground state separated by about 40 K (3.45 meV) from a doublet as the first excited state. However, the CEF parameters for

Table 4. CEF parameters (B_{nm}), eigenfunctions (Γ_i), energies (E_i), and transition probabilities ($|\langle\Gamma_i|J_\perp|\Gamma_j\rangle|^2$) for $CePd_2Al_3$ obtained by an extrapolation from those of $NdPd_2Al_3$. Bold numbers correspond to CEF transitions with zero energy transfer.

CEF parameters B_{nm}:	(Extrapolation)		
B_{20} (10^1 meV)	0.228 ± 0.005		
B_{40} (10^{-1} meV)	0.329 ± 0.007		
B_{60} (meV)	0		
B_{66} (meV)	0		
Eigenfunctions Γ_i:	Energies E_i (meV):		
(extrapolated)	(extrapolated)	(neutron [12])	(χ [11])
$\Gamma_8 = \|\pm 5/2\rangle$	39.1 ± 0.9	—	≈ 68.9
$\Gamma_9 = \|\pm 3/2\rangle$	3.8 ± 0.4	2.95	2.84
$\Gamma_7 = \|\pm 1/2\rangle$	0	0	0
Transition probabilities $\|\langle\Gamma_i\|J_\perp\|\Gamma_j\rangle\|^2$:			
(extrapolated)	Γ_7	Γ_9	Γ_8
E (meV)	0	3.8	39.1
Γ_8			**8.33**
Γ_9		**3.00**	3.33
Γ_7	**6.33**	5.33	0

$PrPd_2Al_3$, tentatively derived from powder magnetic susceptibility data [5], give rise to a magnetically easy c-axis with a CEF ground-state singlet Γ_4 and a first-excited-state singlet Γ_3 at 22 K (1.89 meV), which turns out to be incompatible with our neutron scattering data. This is not surprising, since powder susceptibility data alone are insensitive to the details of the CEF level structure.

3.3. Extrapolation to $CePd_2Al_3$

For $CePd_2Al_3$, the CEF Hamiltonian (1) splits the sixfold-degenerate ground-state J-multiplet $^2F_{5/2}$ of Ce^{3+} into three doublets ($\Gamma_7, \Gamma_8, \Gamma_9$). The extrapolation (4) with no adjustable parameter yields the CEF level diagram shown in figure 8 with the CEF parameters, eigenfunctions, energies, and transition probabilities given in table 4. The single-crystal magnetic susceptibility χ of $CePd_2Al_3$ [11] can be satisfactorily described by a CEF ground state Γ_7, and excited states Γ_9 at 33 K (2.84 meV) and Γ_8 at $\approx$800 K ($\approx$68.9 meV). Our extrapolation (figure 8) yields a similar CEF level sequence, $\Gamma_7 \rightarrow \Gamma_9 \rightarrow \Gamma_8$, for $CePd_2Al_3$, but—compared to the analysis of the susceptibility data—the excitation energies are predicted to be (34 ± 14)% larger for $\Gamma_7 \rightarrow \Gamma_9$ and $\approx$41% smaller for $\Gamma_9 \rightarrow \Gamma_8$. For $CePd_2Al_3$, the relevant energy scales have been estimated from bulk measurements [3, 4] to be the Néel temperature $T_N = 2.8$ K, the Kondo temperature $T_K = 19$ K, and the CEF splitting $\Gamma_7 \rightarrow \Gamma_9$ at $\Delta_1 = 33$ K. Since Δ_1 and T_K are close together, the $\Gamma_7 \rightarrow \Gamma_9$ CEF excitation, measured by means of inelastic neutron scattering [12], appears as a broad feature with a Lorentzian peak shape. At $T = 12$ K, the position of the maximum at 2.95 meV gives rise to $\Delta_1 = 34$ K, and the width, extrapolated to $T = 0$ K, of 1.92 meV corresponds to $T_K = 22$ K. The values for Δ_1 and for T_K obtained from neutron scattering data and from bulk measurements are in excellent agreement. But the larger value, $\Delta_1 = 3.8(4)$ meV, from our extrapolation (figure 8) lies well inside the

broad neutron peak, with a width of 2.2 meV at 12 K and 4.0 meV at 100 K. In addition, the extremely large overall CEF splitting of ≈800 K for $CePd_2Al_3$ suggested by susceptibility data [11] remains to be verified by means of a direct spectroscopic measurement. So far, inelastic neutron scattering experiments [12] have failed to observe the broadened $\Gamma_9 \rightarrow \Gamma_8$ CEF transition.

Similar to that of $NdPd_2Al_3$ the CEF ground state of $CePd_2Al_3$ is the doublet Γ_7, with expected ordered moments of 1.29 μ_B for the basal plane and 0.43 μ_B parallel to the *c*-axis. The magnetic anisotropy of Γ_7 fixes the directions of the antiferromagnetically ordered Ce moments into the basal plane, and a rather strong Kondo effect is responsible for the reduction of the observed saturation moment $\mu_0(\mathrm{Ce}) = 0.47(2)\ \mu_B$ [10], to below the value 1.29 μ_B expected for Γ_7.

The representations Γ_i used in this work (tables 2–4) correspond to the notation of Koster *et al* [18], and have been verified by calculating the characters (see table 72 in [18]) for all of the CEF eigenfunctions of Ce^{3+}, Pr^{3+}, and Nd^{3+}.

4. Conclusions

By means of powder neutron scattering and single-crystal susceptibility experiments on $NdPd_2Al_3$, we have been able to unambiguously determine the values of all four CEF parameters (B_{20}, B_{40}, B_{60}, B_{66}). The resulting CEF level diagram of $NdPd_2Al_3$ shown in figure 2: (i) is compatible with the excitation energies and intensities of the CEF transitions observed by means of neutron spectroscopy; (ii) can reproduce the behaviour and anisotropy of the single-crystal susceptibility; and (iii) can explain the directions and sizes of the antiferromagnetically ordered Nd moments at saturation reasonably well.

The CEF parameters obtained for $NdPd_2Al_3$ are extrapolated to those for the isostructural compounds $PrPd_2Al_3$ and $CePd_2Al_3$. For $PrPd_2Al_3$, the powder neutron scattering measurement of the two strongest CEF excitations $\Gamma_1 \rightarrow \Gamma_5$ and $\Gamma_5 \rightarrow \Gamma_6^{(1)}$ confirms the reliability of the extrapolated CEF level diagram shown in figure 8, with an accuracy of better than 10% for the excitation energies. Since the CEF ground-state singlet Γ_1 is separated by 64 K from the first-excited-state doublet Γ_5, no magnetic ordering is expected for $PrPd_2Al_3$ down to the lowest temperatures. For $CePd_2Al_3$, the extrapolation yields the same CEF level sequence (see figure 8) as has been derived from single-crystal susceptibility data [11]. The magnetic anisotropy of the CEF ground state Γ_7 is compatible with the realized magnetic structure [10]. In $CePd_2Al_3$, a rather strong Kondo effect causes a significant reduction of the antiferromagnetically ordered Ce moment to below the value expected from Γ_7, and in addition gives rise to a broadening of the CEF transitions. The predicted $\Gamma_7 \rightarrow \Gamma_9$ excitation energy lies well inside the width of the broad inelastic magnetic peak observed by neutron scattering [12].

An extrapolation from $NdPd_2Al_3$ to $SmPd_2Al_3$ with the use of equation (4) yields a CEF splitting of the lowest-lying *J*-multiplet $^6H_{5/2}$ of Sm^{3+} into a ground-state doublet $\Gamma_8 = |\pm 5/2\rangle$, and excited-state doublets $\Gamma_9 = |\pm 3/2\rangle$ at 12.9 ± 0.3 meV and $\Gamma_7 = |\pm 1/2\rangle$ at 22.3 ± 0.5 meV, which implies a magnetically easy *c*-axis. However, according to a very recent single-crystal magnetic susceptibility experiment [8], magnetism in $SmPd_2Al_3$ is more complicated, and the easy direction of magnetization changes at 37 K from the expected *c*-axis at lower temperatures to inside the *ab*-plane at higher temperatures.

Acknowledgment

Financial support from the Swiss National Science Foundation is gratefully acknowledged.

References

[1] Geibel C, Schank C, Thies S, Kitazawa H, Bredl C D, Böhm A, Rau M, Grauel A, Caspary R, Helfrich R, Ahlheim U, Weber G and Steglich F 1991 *Z. Phys.* B **84** 1
[2] Krimmel A, Fischer P, Roessli B, Maletta H, Geibel C, Schank C, Grauel A, Loidl A and Steglich F 1992 *Z. Phys.* B **86** 161
[3] Kitazawa H, Schank C, Thies S, Seidel B, Geibel C and Steglich F 1992 *J. Phys. Soc. Japan* **61** 1461
[4] Mentink S A M, Bos N M, Nieuwenhuys G J, Drost A, Frikkee E, Tai L T, Menovsky A A and Mydosh J A 1993 *Physica* B **186–188** 497
[5] Ghosh K, Ramakrishnan S, Malik S K and Chandra G 1993 *Phys. Rev.* B **48** 6249
[6] Dönni A, Kitazawa H, Fischer P, Vogt T, Matsushita A, Iimura Y and Zolliker M 1996 *J. Solid State Chem.* **127** 169
[7] Kitazawa H, Mori A, Takano S, Yamadaya T, Matsushita A and Matsumoto T 1993 *Physica* B **186–188** 661
[8] Kitazawa H 1997 unpublished results
[9] Colineau E, Sanchez J P, Rebizant J and Winand J M 1994 *Solid State Commun.* **92** 915
[10] Dönni A, Fischer P, Roessli B and Kitazawa H 1994 *Z. Phys.* B **93** 449
[11] Mentink S A M, Nieuwenhuys G J, Menovsky A A, Mydosh J A, Tou H and Kitaoka Y 1994 *Phys. Rev.* B **49** 15759
[12] Mentink S A M, Nieuwenhuys G J, Menovsky A A, Mydosh J A, Drost A, Frikkee E, Bando Y, Takabatake T, Böni P, Fischer P, Furrer A, Amato A and Schenck A 1994 *Physica* B **199+200** 143
[13] Stevens K W H 1952 *Proc. Phys. Soc.* A **65** 209
[14] Trammel G T 1953 *Phys . Rev.* **92** 1387
[15] Dunlap B D, Hall L N, Behroozi F, Crabtree G W and Niarchos D G 1984 *Phys. Rev.* B **29** 6244
[16] Fulde P 1979 *Handbook on the Physics and Chemistry of Rare Earths* ed K A Gschneidner and L Eyring Jr (Amsterdam: North-Holland) p 295
[17] Ghosh K, Ramakrishnan S, Chinchure A D, Marathe V R and Chandra G 1996 *Physica* B **223+224** 354
[18] Koster G F, Dimmock J O, Wheeler R G and Statz H 1963 *Properties of the Thirty-two Point Groups* (Cambridge, MA: MIT Press)